
Long-term simulation of large deformation, mechano-chemical fluid-structure interactions in ALE and fully Eulerian coordinates

Stefan Frei, Thomas Richter, Thomas Wick

Institute for Applied Mathematics
Heidelberg University, 69120 Heidelberg, Germany

Department of Mathematics, AM3
FAU Erlangen-Nürnberg, 91058 Erlangen, Germany

Johann Radon Institute for Computational
and Applied Mathematics (RICAM)
Austrian Academy of Sciences
Altenberger Str. 69, 4040 Linz, Austria

Accepted for publication in
Journal of Computational Physics (JCP)
in June 2016

DOI: <https://doi.org/10.1016/j.jcp.2016.06.015>

©2016. This manuscript version is made available under the
CC-BY-NC-ND 4.0 license

<https://creativecommons.org/licenses/by-nc-nd/4.0/>

Long-term simulation of large deformation, mechano-chemical fluid-structure interactions in ALE and fully Eulerian coordinates

S. Frei^a, T. Richter^{b,*}, T. Wick^{c,d}

^a*Institute for Applied Mathematics, Heidelberg University, 69120 Heidelberg, Germany*

^b*Department of Mathematics, AM3, FAU Erlangen-Nürnberg, 91058 Erlangen, Germany*

^c*Johann Radon Institute for Computational and Applied Mathematics (RICAM)*

Austrian Academy of Sciences, Altenberger Str. 69, 4040 Linz, Austria

^d*Fakultät für Mathematik, Lehrstuhl M17*

Technische Universität München, 85747 Garching bei München, Germany

Abstract

In this work, we develop numerical schemes for mechano-chemical fluid-structure interactions with long-term effects. We investigate a model of a growing solid interacting with an incompressible fluid. A typical example for such a situation is the formation and growth of plaque in blood vessels. This application includes two particular difficulties: First, growth may lead to very large deformations, up to full clogging of the fluid domain. We derive a simplified set of equations including a fluid-structure interaction system coupled to an ODE model for plaque growth in Arbitrary Lagrangian Eulerian (ALE) coordinates and in Eulerian coordinates. The latter novel technique is capable of handling very large deformations up to contact. The second difficulty stems from the different time scales: while the dynamics of the fluid demand to resolve a scale of seconds, growth typically takes place in a range of months. We propose a temporal two-scale approach using local small-scale problems to compute an effective wall stress that will enter a long-scale problem. Our proposed techniques are substantiated with several numerical tests that include comparisons of the Eulerian and ALE approaches as well as convergence studies.

Keywords: finite elements, fluid-structure interaction, solid growth, fully Eulerian approach, arbitrary Lagrangian-Eulerian approach, temporal multi-scales

*Corresponding author

Email addresses: stefan.frei@iwr.uni-heidelberg.de (S. Frei), richter@math.fau.de (T. Richter), wick@ma.tum.de (T. Wick)

1. Introduction

In this article, we tackle fundamental problems of chemically reacting fluid-structure interactions (FSI) and design numerical approximation schemes specially suited to challenging applications. The prototypical application under consideration is the formation and growth of plaques in blood vessels. Typical challenges are threefold: first, a large coupled system of reaction, fluid- and solid-dynamics. Second, very large deformation up to a clogging of blood vessels. Third, the necessity to incorporate a wide range of time-scales, which includes the mechanical dynamics of the pulsating heart flow (< 1 s) and ranges up to several months, the typical scale for plaque growth. Another application (with small deformation, however) is the investigation of chemical flows in pipelines, where long-time effects of weathering, accelerated by the transported substances, cause material alteration. Although we focus on plaque formation, the numerical schemes presented in this paper cover a wider and more general scope.

To face the different challenges, we need a method that is able to handle large deformations and secondly, that can incorporate the range of temporal scales. Numerically, this second request demands for robust implicit discretization schemes, which allow to use large time-steps. In terms of fluid-structure interactions, only monolithic formulations allow for strictly implicit schemes. In biomedical applications, monolithic schemes are preferable anyway, as the stiff coupling coming from similar densities of blood and tissue, known as the added-mass effect [12], calls for strongly coupled methods.

In general, FSI methods are classified into interface-tracking and interface-capturing methods. The most popular interface-tracking methods are ALE-type (arbitrary Lagrangian-Eulerian) approaches [27, 17, 40, 41]. On the other hand, with interface-capturing methods, the interface is typically not resolved by the mesh geometry [5, 32, 19, 16]. These approaches are usually not restricted by the extent of the deformation. Also, contact and topology changes might be incorporated [35, 46]. On the downside, interface-capturing methods suffer from a reduced accuracy at the interface, as it cannot be resolved by standard discretization methods. Both the spatial and the temporal discretization is a challenge. For spatial discretization, interface-capturing methods are often combined with enriched or modified finite elements schemes [24, 33, 23] or they incorporate a coupling based on Nitsche's method [25, 10].

Among the multitude of different approaches, we apply the fully Eulerian method [19, 36] together with a locally modified parametric finite element scheme [22], which accurately resolves the moving interface without the need of remeshing and without adding new degrees of freedom. For validation, we derive the complete system of equations including solid growth also in ALE coordinates. We present simulation results for both an ALE and a fully Eulerian approach.

For modeling of chemically induced material alteration and growth we follow the work of Rodriguez et al. [37]. We use a multiplicative decomposition of the deformation gradient into an elastic part and an active part that describes the growth and depends on the concentration of chemical species (see also [30]).

To describe plaque growth, we introduce a simplified system, which is based

on a detailed model coupling fluid-structure interactions with active growth and a chemical reaction system. The latter one describes the migration of monocytes through the vessel walls and the deformation into macrophages in foam cells, which finally cause growth and deformation and alteration of the vessel walls [50]. The plaque formation model is significantly simplified as only homogeneous tissue material and a Newtonian model for blood flow are considered. The chemical system describing transformation and growth processes is reduced to a single scalar ordinary differential equation (ODE). One consequence of these simplifications is that they prevent a direct comparison to experimental or clinical results.

Simulations of plaque growth must extend over large periods of time. The migration rate of monocytes, however, is strongly influenced by the hemodynamical forces on the vessel walls. These depend significantly on the pulsation of the blood flow. A direct simulation that resolves this short time scale and that covers a period of months is out of bounds. This very fundamental problem occurs in various applications, such as the mechanical weathering of constructions induced by the periodic cycles of day and night (due to temperature effects). A detailed and generic analysis as well as efficient numerical tools are still missing.

For plaque formation, most approaches use an averaging in time and focus on the long-scale dynamics only [13, 50]. In the present paper, we present a new technique, that employs the solution of short-term systems, which resolve the pulsation of the flow in order to determine an effective parameter, namely the wall stress in main stream direction. Numerical simulations in Section 5.2 will show, that the incorporation of these fine scales has a considerable effect on the overall dynamics. Secondly, we formulate the coupled problem in Eulerian coordinates to allow for large deformation and growth of plaques up to a complete clogging of the vessel. This Eulerian formulation of a fluid-structure interaction problem with chemically induced growth is not restricted to plaque growth but might be applied in various applications.

The organization of our article is as follows: In Section 2, we introduce the coupled model for mechano-chemical fluid-structure interactions based on a simplified model for plaque growth. We formulate a long-scale problem for the coupled FSI-growth dynamics as well as a short-scale problem that will serve to estimate an effective wall stress. Furthermore, we briefly recapitulate the Eulerian formulation of the coupled set of equations. In Section 3, we derive the monolithic variational formulations in ALE and fully Eulerian coordinates. Section 4 gives a short overview of the discretization techniques used to approximate the differential equations. We present numerical results that allow us to compare the different modeling schemes in Section 5. Finally, we conclude in Section 6.

2. Modeling

We introduce a simplified model that describes the formation and growth of plaques in large blood vessels. For simplicity, we denote by $\Omega(t) \subset \mathbb{R}^2$ a two-dimensional domain, split into the vessel wall $\mathcal{S}(t) \subset \mathbb{R}^2$ and the fluid domain $\mathcal{F}(t) \subset \mathbb{R}^2$, occupied by blood. The interface between fluid and solid is

denoted by $\Gamma_i(t)$, see Figure 1. We model blood as an incompressible, isothermal, Newtonian and homogeneous fluid, see e.g., [21]. The vessel wall is described by the St. Venant Kirchhoff material law [14]. These models must be considered as simplification suitable for the study at hand. For advanced modeling of hemodynamical configurations, we refer to the literature [26, 29, 21]. Growth of the solid is modeled by a multiplicative decomposition of the deformation gradient, see [37] and Section 2.3.

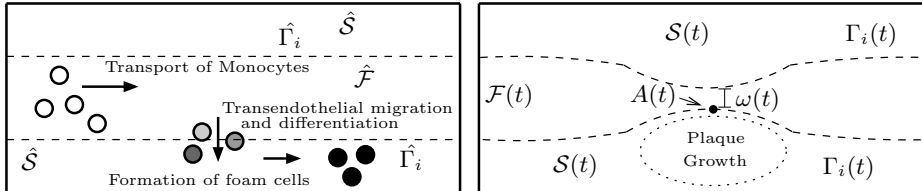


Figure 1: Configuration of the domain and mechanism of plaque formation. Left: Domain in reference configuration split into fluid part $\hat{\mathcal{F}}$ and solid $\hat{\mathcal{S}}$ divided by the interface $\hat{\Gamma}_i$. Right: Domain in the current (Eulerian) description with plaque formation and narrowing of the vessel.

2.1. Modeling of plaque growth

For a derivation of the full model describing the bio-medical background and the mechano-chemical dynamics of plaque formation and plaque growth, we refer to [42, 48, 49, 50] and the references therein. In short, the biological mechanism is evolving as follows (compare Figure 1): First, monocytes are transported by an advection-diffusion process within the blood flow. Secondly, they penetrate damaged parts of the vessel wall where they are transformed to macrophages. The migration rate depends on the wall stress and the damage condition of the wall. Thirdly, within the vessel wall, the macrophages are transformed into foam cells (called c_s). Finally, accumulation of foam cells leads to plaque growth. This mechano-chemical process involves a large variety of different coupled effects such as geometrical deformations, mechanical remodeling and alteration of blood and tissue behavior. Most of these effects are not completely understood. We refer to the works of Ambrosi, Humphrey et al. [1, 28] and the literature cited therein for detailed modeling of growth and remodeling in vascular mechanics.

The process of plaque formation is coupled to the dynamics of the fluid-structure interaction problem. Due to hemodynamical forces driven by the pulsating flow, the geometry deforms substantially. Furthermore, the formation of plaques significantly changes the domains. Finally, the hemodynamical forces influence the penetration of monocytes into the vessel wall and therefore a two-way coupled problem must be considered. The complete set of equations is

given by

$$\begin{aligned}
& \left. \begin{aligned} \rho_f(\partial_t \mathbf{v}_f + \mathbf{v}_f \cdot \nabla \mathbf{v}_f) - \operatorname{div} \boldsymbol{\sigma}_f &= 0 \\ \operatorname{div} \mathbf{v}_f &= 0 \end{aligned} \right\} \text{in } \mathcal{F}(t), \\
& \left. \begin{aligned} \rho_s(\partial_t \mathbf{v}_s + \mathbf{v}_s \cdot \nabla \mathbf{v}_s) - \operatorname{div} \boldsymbol{\sigma}_s(c_s) &= 0 \\ \partial_t \mathbf{u}_s + \mathbf{v}_s \cdot \nabla \mathbf{u}_s - \mathbf{v}_s &= 0 \\ \partial_t c_s &= \gamma(\boldsymbol{\sigma}_{WS}) \end{aligned} \right\} \text{in } \mathcal{S}(t), \\
& \left. \begin{aligned} \boldsymbol{\sigma}_f \vec{n}_f + \boldsymbol{\sigma}_s \vec{n}_s &= 0 \\ \mathbf{v}_f &= \mathbf{v}_s \end{aligned} \right\} \text{on } \Gamma_i(t).
\end{aligned} \tag{1}$$

Here, \mathbf{v}_f and \mathbf{v}_s stand for the fluid and solid velocity. By ρ_f and ρ_s we denote the densities of blood and of the vessel wall and by \vec{n}_f and \vec{n}_s the outer normals of the fluid and solid domain, respectively. The solid growth in (1) depends on the concentration of foam cells c_s and enters the equation via the solid stress tensor $\boldsymbol{\sigma}_s$. The concentration of foam cells c_s , on the other hand, depends on the fluid wall stress σ_{WS} as described below. Models for the material laws for the stress tensors $\boldsymbol{\sigma}_f$ and $\boldsymbol{\sigma}_s$ including solid growth will be given in Section 2.3.

For modeling the accumulation of foam cells c_s in (1), we consider the simplified ODE model

$$\gamma(\boldsymbol{\sigma}_{WS}) = \gamma_0 \left(1 + \frac{\boldsymbol{\sigma}_{WS}}{\bar{\boldsymbol{\sigma}}} \right)^{-1}, \quad \bar{\boldsymbol{\sigma}} = \frac{50 \text{ g}}{\text{cm} \cdot \text{s}^2}, \quad \gamma_0 = 5 \cdot 10^{-7}, \tag{2}$$

where by $\boldsymbol{\sigma}_{WS}$ we denote the mean wall stress in the main flow direction, averaged over the entire fluid-structure interface (see Figure 1)

$$\boldsymbol{\sigma}_{WS} = \int_{\Gamma_i} |\boldsymbol{\sigma}_f \vec{n}_f \cdot \vec{e}_1| \, d\sigma. \tag{3}$$

The exact role and influence of the wall stress on the migration rate is not yet completely understood. For a further discussion, we refer to [7, 15]. Growth - depending on c_s - will take part in the middle part of the vessel walls, see Figure 1 and Section 5 for details. Rather than developing a quantitative model, we concentrate in this paper on a robust numerical framework for the coupled long-term dynamics of fluid-structure interaction with active growth processes and large deformation. Hence, the approximation of the chemical dynamics play a minor role.

2.2. Separation of the temporal scales

One of the major challenges in plaque modeling are the different time scales: while the heart beats once in about every 1 s, plaque growth takes place in a time span of months, i.e. $> 1\,000\,000$ s. Although all scales have a significant influence on the coupled dynamics, a numerical simulation will not be able to resolve each detail while following the long-term process. Instead, we - as most approaches - consider an averaged flow problem and focus on the long-scale dynamics of (2).

To incorporate the effects of the short-scale dynamics, we compute effective wall stresses with the help of isolated small-scale simulations.

Accurate handling of the different time-scales is an open problem. Most approaches use an averaging in time and focus only on the long-scale dynamics [13, 50]. Here, we will introduce two different models: first a long-scale problem, that basically corresponds to the averaging approaches found in literature. The long-scale time variable is denoted by τ , measured in units of days. Secondly, we introduce local short-scale problems resolving the pulsating flow in a short time scale denoted by t , measured in seconds. These problems will be used to compute an effective wall stress guiding the long-scale computations.

Remark 1 (Partitioning of the temporal scales). *To separate the long-scale problem from the short-scale influence, we make the following assumptions: considering the long scale τ (days), dynamic effects of the mechanical fluid-structure interaction system do not play a role. Instead, fluid and solid are assumed to be in a stationary limit. As the long-scale problem cannot resolve the pulsating flow, a time-averaged inflow velocity $\bar{\mathbf{v}}^{in}$ is taken as boundary condition. The only remaining temporal effect in the long-scale problem is that of the evolving chemical dynamics causing material growth.*

The short-scale effect is given by the nonlinear dynamics of the pulsating blood flow on the effective wall stress. We assume, that during the short time-period $[\tau \text{ (days)}, \tau \text{ (days)} + \delta t \text{ (s)}]$ (where δt is a time span of the short-scale problem, e.g. the time of 3 heart beats), no significant change in chemistry (growth) takes place. Furthermore, we assume, that the influence of the short-scale dynamics on the initial condition is small. This is important, as exact initial data is not available for isolated short-scale problems. This assumption is justified by the damping of the viscous fluid.

By the assumptions outlined in Remark 1, we can formulate the long-scale problem including growth:

Problem 1 (Long-Scale Growth). *In $I = [0, T \text{ days}]$, find fluid-velocity \mathbf{v}_f , pressure p_f , solid deformation \mathbf{u}_s and foam cell concentration c_s , given by*

$$\begin{aligned} \rho_f \mathbf{v}_f \cdot \nabla \mathbf{v}_f - \operatorname{div} \boldsymbol{\sigma}_f &= 0, & \operatorname{div} \mathbf{v}_f &= 0 & \text{in } \mathcal{F}(\tau) \\ & & - \operatorname{div} \boldsymbol{\sigma}_s(c_s) &= 0 & \text{in } \mathcal{S}(\tau) \\ \mathbf{v}_f &= 0, & \boldsymbol{\sigma}_f \bar{\mathbf{n}}_f + \boldsymbol{\sigma}_s(c_s) \bar{\mathbf{n}}_s &= 0 & \text{on } \Gamma_i(\tau) \\ \partial_\tau c_s &= \gamma(\boldsymbol{\sigma}_{WS}), & c_s(0) &= 0 & \text{in } \mathcal{S}(\tau). \end{aligned} \quad (4)$$

The boundary data is given by

$$\mathbf{v}_f = \bar{\mathbf{v}}^{in} \text{ on } \Gamma_f^{in}, \quad \rho_f \nu_f \bar{\mathbf{n}} \cdot \nabla \mathbf{v}_f - p_f \bar{\mathbf{n}} = 0 \text{ on } \Gamma_f^{out}, \quad \mathbf{u}_s = 0 \text{ on } \Gamma_s, \quad (5)$$

where $\bar{\mathbf{n}}$ is the outward facing normal vector and $\bar{\mathbf{v}}^{in}$ is an averaged inflow profile that depends on the width of the blood vessel and that will be specified in Section 5. The average inflow rate reflects the average blood-flow during one cardiac cycle.

As second problem, we consider the short-scale problem of a pulsating flow. Here, we assume, that the time-scale is so short (some few cycles of the pulsation, e.g. $\delta t \approx 3\text{s}$), that further growth can be neglected. Hence, at time τ we freeze the growth and consider the problem:

Problem 2 (Short-Scale Pulsation). For $\tau \geq 0$ days let $c_s(\tau)$ be given. In $I^* = [\tau \text{ days}, \tau \text{ days} + \delta t \text{ s}]$ find fluid-velocity \mathbf{v}_f , pressure p_f , solid deformation \mathbf{u}_s and velocity \mathbf{v}_s , given by

$$\begin{aligned} \rho_f(\partial_t \mathbf{v}_f + \mathbf{v}_f \cdot \nabla \mathbf{v}_f) - \operatorname{div} \boldsymbol{\sigma}_f &= 0, \quad \operatorname{div} \mathbf{v}_f = 0 \quad \text{in } \mathcal{F}(t) \\ \rho_s(\partial_t \mathbf{v}_s + \mathbf{v}_s \cdot \nabla \mathbf{v}_s) - \operatorname{div} \boldsymbol{\sigma}_s(c_s(\tau)) &= 0, \quad \partial_t \mathbf{u}_s + \mathbf{v}_s \cdot \nabla \mathbf{u}_s - \mathbf{v}_s = 0 \quad \text{in } \mathcal{S}(t) \\ \mathbf{v}_f &= \mathbf{v}_s, \quad \boldsymbol{\sigma}_f \vec{n}_f + \boldsymbol{\sigma}_s(c_s(\tau)) \vec{n}_s = 0 \quad \text{on } \Gamma_i(t). \end{aligned} \quad (6)$$

The boundary data is given by:

$$\mathbf{v}_f(t) = \mathbf{v}^{in}(t) \text{ on } \Gamma_f^{in}, \quad \rho_f \nu_f \vec{n} \cdot \nabla \mathbf{v}_f - p_f \vec{n} = 0 \text{ on } \Gamma_f^{out}, \quad \mathbf{u}_s = 0 \text{ on } \Gamma_s, \quad (7)$$

where $\mathbf{v}^{in}(t)$ is a pulsating velocity profile, that depends on the width of the blood vessel and will be specified in Section 5.

The idea behind this two-level approach is to use the short-scale problem for the determination of an effective wall stress entering the long-scale problem. New coefficients must be computed, whenever the growth led to a significant modification of the geometry. An automatic feedback approach is possible by means of model error estimation, see [6]. This, however, is subject to current research.

2.3. Material laws and modeling of growth

We model blood as an incompressible Newtonian fluid, such that the Cauchy stresses are given as

$$\boldsymbol{\sigma}_f = \rho_f \nu_f (\nabla \mathbf{v}_f + \nabla \mathbf{v}_f^T) - pI, \quad (8)$$

where by ρ_f we denote the density and by ν_f the kinematic viscosity of blood.

For the vessel wall, we consider the Saint Venant-Kirchhoff model, with the 1st Piola-Kirchhoff stress $\hat{\mathbf{P}}_e = \hat{\mathbf{F}}_e \hat{\boldsymbol{\Sigma}}_e$:

$$\hat{\mathbf{P}}_e = 2\mu_s \hat{\mathbf{F}}_e \hat{\mathbf{E}}_e + \lambda_s \hat{\mathbf{F}}_e \operatorname{tr}(\hat{\mathbf{E}}_e) I, \quad \hat{\mathbf{E}}_e := \frac{1}{2}(\hat{\mathbf{F}}_e^T \hat{\mathbf{F}}_e - I), \quad (9)$$

where the hats indicate, that all these quantities are given in the Lagrangian reference system. By $\hat{\mathbf{F}}_e$, we denote the elastic deformation gradient that will be specified below, by μ_s and λ_s the Lamé material parameters.

For incorporating growth, we follow the ideas of Rodriguez and co-workers [37]. We shortly recapitulate this concept and refer the reader to Figure 2. By \hat{V} we denote the Lagrangian, stress-free and growth-free reference system. By \hat{V}_g we denote an intermediate system, that results from active growth. \hat{V}_g can be considered as stress-free, but as non-physical, as growth results in an overlapping

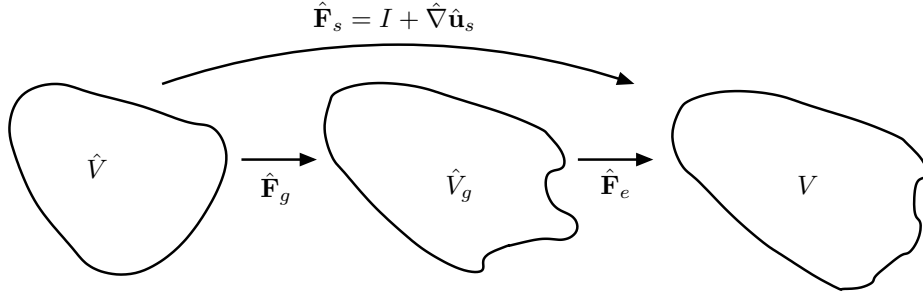


Figure 2: Volume elements \hat{V}, \hat{V}_g, V and deformation gradients linking them. \hat{V} denotes the stress-free Lagrangian configuration, \hat{V}_g an intermediate (non-physical) configuration after growth and V the current volume element.

of control volumes. Finally, V is the current configuration which is stress-loaded and which is physically adjusted to the grown intermediate configuration. The deformation $\hat{\mathbf{u}}_s$ describes the full transition from \hat{V} to V :

$$\hat{T}_s := \text{id} + \hat{\mathbf{u}}_s : \hat{V} \rightarrow V, \quad \hat{\mathbf{F}}_s := \hat{\nabla} \hat{T}_s = I + \hat{\nabla} \hat{\mathbf{u}}_s \quad (10)$$

where id denotes the identity. By \hat{T}_g we denote the transition caused by active growth

$$\hat{T}_g : \hat{V} \rightarrow \hat{V}_g, \quad \hat{\mathbf{F}}_g := \hat{\nabla} \hat{T}_g. \quad (11)$$

As \hat{V}_g is considered to be stress-free, the elastic response is only based on the mapping T_e between \hat{V}_g and V

$$\hat{T}_e : \hat{V}_g \rightarrow V, \quad \hat{\mathbf{F}}_e := \hat{\nabla} \hat{T}_e, \quad (12)$$

see also Figure 2. Given a growth model \hat{T}_g , the elastic deformation gradient $\hat{\mathbf{F}}_e$ can be computed from the total deformation gradient $\hat{\mathbf{F}}_s = I + \hat{\nabla} \hat{\mathbf{u}}_s$ by

$$\hat{\mathbf{F}}_s = \hat{\mathbf{F}}_e \hat{\mathbf{F}}_g \Leftrightarrow \hat{\mathbf{F}}_e = \hat{\mathbf{F}}_s \hat{\mathbf{F}}_g^{-1} = [I + \hat{\nabla} \hat{\mathbf{u}}_s] \hat{\mathbf{F}}_g^{-1}. \quad (13)$$

In this article, we use an isotropic growth tensor $\hat{T}_g(\tau) : \hat{V} \rightarrow \hat{V}_g$ such that with (13) it follows that

$$\hat{\mathbf{F}}_g = \hat{g}I \Rightarrow \hat{\mathbf{F}}_e := \hat{g}^{-1} \hat{\mathbf{F}}_s. \quad (14)$$

Here, $\hat{g} = \hat{g}(\hat{\mathbf{x}}, \tau)$ is a scalar function depending on the concentration of foam cells c_s that will be specified in Section 5. $\hat{g}(\hat{\mathbf{x}}, \tau)$ varies in the long time-scale τ (days).

Altogether, the elastic Green Lagrange strain is given by

$$\hat{\mathbf{E}}_e = \frac{1}{2}(\hat{\mathbf{F}}_e^T \hat{\mathbf{F}}_e - I) = \frac{1}{2}(\hat{g}^{-2} \hat{\mathbf{F}}_s^T \hat{\mathbf{F}}_s - I) \quad (15)$$

resulting in the Piola-Kirchhoff stresses

$$\hat{\mathbf{F}}_e \hat{\Sigma}_e = \hat{\mathbf{P}}_e = 2\mu_s \hat{\mathbf{F}}_e \hat{\mathbf{E}}_e + \lambda_s \text{tr}(\hat{\mathbf{E}}_e) \hat{\mathbf{F}}_e = 2\mu_s \hat{g}^{-1} \hat{\mathbf{F}}_s \hat{\mathbf{E}}_e + \lambda_s \hat{g}^{-1} \text{tr}(\hat{\mathbf{E}}_e) \hat{\mathbf{F}}_s. \quad (16)$$

3. Monolithic schemes for the coupled problem

In this section, we derive monolithic variational formulations for Problems 1 and 2. For both of these problems we will derive two formulations, first, in Section 3.1 based on arbitrary Lagrangian-Eulerian coordinates (ALE). Second, in Section 3.2 we derive the variational formulation in fully Eulerian coordinates.

In ALE formulations, the fluid problem is mapped onto a fixed reference system $\hat{\mathcal{F}}$ that matches the Lagrangian solid system on $\hat{\Gamma}_i$. All the domain motion, whether by growth or elasticity will be implicitly captured in the reference map $\hat{T}_s(t) : \hat{\mathcal{S}} \rightarrow \mathcal{S}(t)$ and the ALE map $\hat{T}_f(t) : \hat{\mathcal{F}} \rightarrow \mathcal{F}(t)$. ALE formulations are well-established and can be regarded as standard formulation for fluid-structure interaction problems (see [18, 9, 8] and the many references cited therein). They have also been applied to plaque growth problems [51].

Second, we propose an alternative formulation, that is based on the Eulerian description of both problems, as formulated in (4) and (6). The Eulerian formulation has the benefit that it can easily handle very large deformations, up to contact. This is usually a weak point of standard ALE formulations if no additional algorithms such as remeshing are used.

From the approximation point of view, the major difference between ALE and Eulerian formulations is the kind of interface representation. In ALE, the interface $\hat{\Gamma}_i$ between fluid and solid is fixed and will not move. It is tracked by the mappings \hat{T}_s and \hat{T}_f and can be resolved by the mesh at all times. This ensures very good approximation properties and it simplifies numerical discretization and solver techniques. In contrast, the Eulerian interface $\Gamma_i(t)$ moves with time and must be captured, as it cannot be resolved exactly within reasonable computational cost. The possibility to cope with very large deformations will come at the cost of approximation quality and ease of discretization.

3.1. The coupled model in ALE coordinates

The idea behind ALE formulations for fluid-structure interaction problems is to couple the solid problem in Lagrangian coordinates to the formulation of the fluid problem on a fixed reference domain. The reference formulation of the solid problem incorporating growth is given as

$$d_t \hat{\mathbf{v}}_s - \widehat{\text{div}}(\hat{\mathbf{F}}_e \hat{\Sigma}_e) = 0, \quad d_t \hat{\mathbf{u}}_s = \hat{\mathbf{v}}_s, \quad (17)$$

where the elastic deformation gradient depends on the growth tensor and is defined in (13).

We denote the fluid reference domain by $\hat{\mathcal{F}}$, and use $\hat{\mathcal{F}} = \mathcal{F}(0)$, the initial fluid domain. By

$$\hat{T}_f(t) : \hat{\mathcal{F}} \rightarrow \mathcal{F}(t), \quad \hat{\mathbf{F}}_f := \widehat{\nabla} \hat{T}_f, \quad \hat{J}_f := \det(\hat{\mathbf{F}}_f), \quad (18)$$

we introduce the ALE-map onto the (moving) Eulerian domain. A hat “ $\hat{\cdot}$ ” will always denote the use of the reference coordinate system in the fluid- and the Lagrangian system in the solid-domain. Given an ALE map \hat{T}_f (we will get back

to the exact definition later), the Navier-Stokes system can be transformed onto the reference domain $\hat{\mathcal{F}}$, see [17, 36]:

$$\hat{J}_f \rho_f \left(\partial_t \hat{\mathbf{v}}_f + \hat{\mathbf{F}}_f^{-1} (\hat{\mathbf{v}}_f - \partial_t \hat{T}_f) \cdot \hat{\nabla} \hat{\mathbf{v}}_f \right) - \widehat{\text{div}}(\hat{J}_f \hat{\boldsymbol{\sigma}}_f \hat{\mathbf{F}}_f^{-T}) = 0, \quad (19)$$

$$\widehat{\text{div}}(\hat{J}_f \hat{\mathbf{F}}_f^{-1} \hat{\mathbf{v}}_f) = 0, \quad (20)$$

and where the Cauchy stresses, in ALE representation are given as

$$\hat{\boldsymbol{\sigma}}_f := \rho_f \nu_f (\hat{\mathbf{F}}_f^{-1} \hat{\nabla} \hat{\mathbf{v}}_f + \hat{\nabla} \hat{\mathbf{v}}_f^T \hat{\mathbf{F}}_f^{-T}) - \hat{p}_f I. \quad (21)$$

Hereby, the reference velocity \hat{v}_f in ALE coordinates is linked to the Eulerian velocity \mathbf{v}_f by the relation

$$\hat{\mathbf{v}}_f(\hat{\mathbf{x}}, t) = \mathbf{v}_f(\mathbf{x}, t), \quad \mathbf{x} = T_f(\hat{\mathbf{x}}, t). \quad (22)$$

The domain $\mathcal{F}(t)$ is not given a priori, but a result of the coupled dynamics. Likewise, the ALE map $\hat{T}_f(t)$ must be implicitly constructed. We introduce an artificial fluid-domain deformation $\hat{\mathbf{u}}_f$ and define

$$\hat{T}_f(\hat{\mathbf{x}}, t) := \hat{\mathbf{x}} + \hat{\mathbf{u}}_f(\hat{\mathbf{x}}, t), \quad (23)$$

where $\hat{\mathbf{u}}_f$ is an extension of $\hat{\mathbf{u}}_s$ from the interface $\hat{\Gamma}_i$ to the fluid-domain. Various approaches for the definition of this ALE extension are discussed in literature [38, 43]. Here, we choose two different realizations. First, the harmonic extension

$$-\hat{\Delta} \hat{\mathbf{u}}_f = 0 \text{ in } \hat{\mathcal{F}}, \quad \hat{\mathbf{u}}_f = \hat{\mathbf{u}}_s \text{ on } \hat{\Gamma}_i, \quad \hat{\mathbf{u}}_f = 0 \text{ on } \partial \hat{\mathcal{F}} \setminus \hat{\Gamma}_i, \quad (24)$$

and second, the biharmonic extension

$$\begin{aligned} \hat{\Delta}^2 \hat{\mathbf{u}}_f &= 0 \text{ in } \hat{\mathcal{F}}, \quad \hat{\mathbf{u}}_f = \hat{\mathbf{u}}_s \text{ and } \hat{n} \cdot \hat{\nabla} \hat{\mathbf{u}}_f = \hat{n} \cdot \hat{\nabla} \hat{\mathbf{u}}_s \text{ on } \hat{\Gamma}_i, \\ \hat{\mathbf{u}}_f &= \hat{n} \cdot \hat{\nabla} \hat{\mathbf{u}}_f = 0 \text{ on } \partial \hat{\mathcal{F}} \setminus \hat{\Gamma}_i. \end{aligned} \quad (25)$$

The harmonic extension can be considered to be the most simple and efficient one. In particular for problems with reentrant edges, however, it often lacks quality. The biharmonic extension on the other hand is usually more costly [47], but yields very good mappings.

Coupling of the Navier-Stokes equations in ALE (19) to the elastic structure equation in Lagrangian formulation (17) is realized by variational principles: velocity, deformation and test-functions are globally defined on $\hat{\Omega}$, such that geometric, kinematic and dynamic conditions are built into the function spaces, see [36].

With these preparations, we can formulate the variational systems of Problems 1 and 2 in ALE coordinates:

Variational Formulation 1 (Long-Scale, ALE). *Find the fluid velocity $\hat{\mathbf{v}}_f \in \bar{\mathbf{v}}^{in}(\tau) + \mathcal{V}_f$, deformation $\hat{\mathbf{u}} \in \mathcal{W}$ and the pressure $\hat{p}_f \in \mathcal{L}_f$, such that*

$$\begin{aligned} (\hat{\rho}_f \hat{J}_f \hat{\mathbf{v}}_f \cdot \hat{\mathbf{F}}_f^{-1} \hat{\nabla} \hat{\mathbf{v}}_f, \hat{\phi}_f)_{\hat{\mathcal{F}}} + (\hat{J}_f \hat{\boldsymbol{\sigma}}_f \hat{\mathbf{F}}_f^{-T}, \hat{\nabla} \hat{\phi})_{\hat{\mathcal{F}}} + (\hat{\mathbf{F}}_e \hat{\boldsymbol{\Sigma}}_e, \hat{\nabla} \hat{\phi})_{\hat{\mathcal{S}}} &= 0 \quad \forall \hat{\phi} \in \mathcal{W}, \\ (\widehat{\text{div}}(\hat{J}_f \hat{\mathbf{F}}_f^{-1} \hat{\mathbf{v}}_f), \hat{\xi}_f)_{\hat{\mathcal{F}}} &= 0 \quad \forall \hat{\xi} \in \mathcal{L}_f, \end{aligned}$$

where the extension $\hat{\mathbf{u}}_f$ is defined as

$$(\hat{\nabla} \hat{\mathbf{u}}_f, \hat{\nabla} \hat{\psi}_f)_{\hat{\mathcal{F}}} = 0 \quad \forall \hat{\psi}_f \in \mathcal{W}_f,$$

in the case of the harmonic extension. For the biharmonic extension, we use

$$(\hat{\mathbf{w}}_f, \hat{\chi}_f)_{\hat{\mathcal{F}}} - (\hat{\nabla} \mathbf{u}_f, \hat{\nabla} \hat{\chi}_f)_{\hat{\mathcal{F}}} + (\hat{\nabla} \hat{\mathbf{w}}_f, \hat{\nabla} \hat{\psi}_f)_{\hat{\mathcal{F}}} = 0 \quad \forall \{\hat{\psi}_f, \hat{\chi}_f\} \in \tilde{\mathcal{W}}_f \times \mathcal{W}_f.$$

The elastic deformation gradient is defined as in (13) depending on the concentration of foam cells. The latter one is defined by the ODE

$$\partial_\tau c_s = \gamma(\boldsymbol{\sigma}_{WS}), \quad c_s(0) = 0.$$

The function spaces are given by

$$\begin{aligned} \mathcal{V}_f &= [H_0^1(\hat{\mathcal{F}}; \hat{\Gamma}_i \cup \hat{\Gamma}_f^{in})]^2, & \mathcal{L}_f &= L^2(\hat{\mathcal{F}}), \\ \mathcal{W} &= [H_0^1(\hat{\Omega}; \hat{\Gamma}_f^{in} \cup \hat{\Gamma}_s)]^2, & \mathcal{W}_f &= [H_0^1(\hat{\mathcal{F}})]^2, & \tilde{\mathcal{W}}_f &= [H^1(\hat{\mathcal{F}})]^2. \end{aligned}$$

Remark 2 (Biharmonic mesh model). We have chosen a mixed formulation for the biharmonic extension, such that an efficient discretization with simple C^0 -conforming finite elements is possible.

Next, and in a similar fashion, we can define the ALE formulation of the short-scale Problem 2:

Variational Formulation 2 (Short-Scale, ALE). For $\tau \geq 0$ days let $c_s := c_s(\tau)$ be given. Find the velocity $\hat{\mathbf{v}} \in \mathbf{v}^{in} + \mathcal{V}$, deformation $\hat{\mathbf{u}} \in \mathcal{W}$ and the pressure $\hat{p}_f \in \mathcal{L}_f$, such that

$$\begin{aligned} (\rho_f \hat{J}_f \hat{\partial}_t \hat{\mathbf{v}}_f, \hat{\phi})_{\hat{\mathcal{F}}} + (\rho_f \hat{J}_f \hat{\nabla} \hat{\mathbf{v}}_f \hat{\mathbf{F}}_f^{-1} (\hat{\mathbf{v}}_f - \partial_t \hat{\mathbf{u}}_f), \hat{\phi})_{\hat{\mathcal{F}}} + (\hat{J}_f \hat{\boldsymbol{\sigma}}_f \hat{\mathbf{F}}_f^{-T}, \hat{\nabla} \hat{\phi})_{\hat{\mathcal{F}}} \\ + (\hat{\rho}_s^0 \hat{\partial}_t \hat{\mathbf{v}}_s, \hat{\phi})_{\hat{\mathcal{S}}} + (\hat{\mathbf{F}}_e(c_s) \hat{\boldsymbol{\Sigma}}_e(c_s), \hat{\nabla} \hat{\phi})_{\hat{\mathcal{S}}} = 0 \quad \forall \hat{\phi} \in \mathcal{W} \\ (\widehat{\text{div}}(\hat{J}_f \hat{\mathbf{F}}_f^{-1} \hat{\mathbf{v}}_f), \hat{\xi}_f)_{\hat{\mathcal{F}}} = 0 \quad \forall \hat{\xi}_f \in \mathcal{L}_f \\ (d_t \hat{\mathbf{u}}_s - \hat{\mathbf{v}}_s, \hat{\psi}_s)_{\hat{\mathcal{S}}} = 0 \quad \forall \hat{\psi}_s \in \mathcal{L}_s. \end{aligned}$$

The extension $\hat{\mathbf{u}}_f$ as well as the function spaces are defined as in Formulation 1. For the velocity, we use the global space

$$\mathcal{V} = [H_0^1(\hat{\Omega}; \hat{\Gamma}_f^{in} \cup \hat{\Gamma}_s)]^2,$$

the test space \mathcal{L}_s is defined by

$$\mathcal{L}_s := L^2(\hat{\Omega}_s).$$

3.2. The coupled model in the fully Eulerian formulation

In this section, we derive an Eulerian formulation of the governing equations. Our approach is based on the fully Eulerian approach presented by Dunne [19] for fluid-structure interactions; see also [20, 35, 44, 36, 39, 31]. Transformation

to the current configuration $\mathcal{S}(t)$ is accomplished by transformation of integrals and derivatives in the variational formulation. First, by $\mathbf{u}_s(\mathbf{x}, t) := \hat{\mathbf{u}}_s(\hat{\mathbf{x}}, t)$ we denote the Lagrangian counterpart of the deformation, such that $\hat{\mathbf{x}} = \mathbf{x} - \mathbf{u}_s(\mathbf{x}, t)$. We denote this mapping by

$$T_s : \Omega(t) \rightarrow \hat{\Omega}, \quad T_s(\mathbf{x}, t) := x - \mathbf{u}_s(\mathbf{x}, t). \quad (26)$$

Furthermore, we denote the deformation gradient by $\mathbf{F}_s := I - \nabla \mathbf{u}_s$ and its determinant by $J_s := \det \mathbf{F}_s$. Applying the chain rule to the relation $T_s \circ \hat{T}_s = \text{id}$, we get the important relation

$$\mathbf{F}_s = \hat{\mathbf{F}}_s^{-1}, \quad J_s = \hat{J}_s^{-1}. \quad (27)$$

As before, the Eulerian deformation gradient is split into a growth part and an elastic part. We denote the inverse mappings of \hat{T}_g and \hat{T}_e by T_g and T_e and their gradients by F_g and F_e respectively. Using relation (27), we have

$$\mathbf{F}_s = \hat{\mathbf{F}}_s^{-1} = \hat{\mathbf{F}}_g^{-1} \hat{\mathbf{F}}_e^{-1} =: \mathbf{F}_g \mathbf{F}_e. \quad (28)$$

Although a direct modeling in Eulerian coordinates is possible, we derive the Eulerian solid model by a mapping of the Lagrangian formulation to the Eulerian system:

$$J_s \hat{\rho}_s^0 (\partial_t \mathbf{v}_s + \mathbf{v}_s \cdot \nabla \mathbf{v}_s) - \text{div} (J_s \mathbf{F}_e^{-1} \boldsymbol{\Sigma}_e \mathbf{F}_s^{-T}) = 0 \quad \text{in } \mathcal{S}(t), \quad (29)$$

$$\partial_t \mathbf{u}_s + \mathbf{v}_s \cdot \nabla \mathbf{u}_s = \mathbf{v}_s$$

where the Eulerian description of the 2nd Piola-Kirchhoff stress is given by

$$\boldsymbol{\Sigma}_e := 2\mu_s \mathbf{E}_e + \lambda_s \text{tr}(\mathbf{E}_e) I, \quad \mathbf{E}_e := \frac{1}{2} (\mathbf{F}_e^{-T} \mathbf{F}_e^{-1} - I). \quad (30)$$

Remark 3 (Piola Transform and Growth). *In (29), we have used the Piola transform $\text{div}(J_s \mathbf{F}_e^{-1} \boldsymbol{\Sigma}_e \mathbf{F}_s^{-T})$ of $\hat{\mathbf{F}}_e \hat{\boldsymbol{\Sigma}}_e$. The determinant J_s as well as the deformation gradient \mathbf{F}_s^{-T} stem from the transformation from the Lagrangian to the Eulerian coordinate system. The Piola transformation can be derived by integral transformation of the variational formulation to the Eulerian system using $\hat{T}(t) : \hat{V} \rightarrow V(t)$:*

$$(\hat{\mathbf{F}}_e \hat{\boldsymbol{\Sigma}}_e, \hat{\nabla} \hat{\phi})_{\hat{\mathcal{S}}} = (J_s \mathbf{F}_e^{-1} \boldsymbol{\Sigma}_e, \nabla \phi \mathbf{F}_s^{-1})_{\mathcal{S}(t)}. \quad (31)$$

By the relations $J_s = J_e J_g$ and $\mathbf{F}_s^{-1} = \mathbf{F}_e^{-1} \mathbf{F}_g^{-1}$, we can define the symmetric Eulerian Cauchy stress tensor of the Saint Venant Kirchhoff solid

$$J_s \mathbf{F}_e^{-1} \boldsymbol{\Sigma}_e \mathbf{F}_s^{-T} = J_g \underbrace{J_e \mathbf{F}_e^{-1} \boldsymbol{\Sigma}_e \mathbf{F}_e^{-T}}_{=: \boldsymbol{\sigma}_e} \mathbf{F}_g^{-T} = J_g \boldsymbol{\sigma}_e \mathbf{F}_g^{-T}. \quad (32)$$

3.2.1. Solid growth in Eulerian coordinates

Next, we carry over the growth model to the Eulerian representation with takes place at the long time scale τ (days). We will use again the simple isotropic growth model

$$\hat{\mathbf{F}}_g = \hat{g}I \quad (33)$$

and define the Eulerian growth function g by setting $g(\mathbf{x}, \tau) = \hat{g}(\hat{\mathbf{x}}, \tau)$. By the relation $\hat{\mathbf{F}}_g = \mathbf{F}_g^{-1}$, it holds that

$$\mathbf{F}_g = g^{-1}I. \quad (34)$$

By the decomposition (28), it follows that

$$\mathbf{F}_e = \mathbf{F}_g^{-1}\mathbf{F}_s = g\mathbf{F}_s, \quad J_e = g^2J_s. \quad (35)$$

The complete Eulerian stresses are given by

$$J_g\boldsymbol{\sigma}_e\mathbf{F}_g^{-T} = J_s\mathbf{F}_e^{-1}\boldsymbol{\Sigma}_e\mathbf{F}_s^{-T} = g^{-1}J_s\mathbf{F}_s^{-1}(2\mu_s\mathbf{E}_e + \lambda_s \text{tr}(\mathbf{E}_e)I)\mathbf{F}_s^{-T}, \quad (36)$$

with the Eulerian elastic strain tensor

$$\mathbf{E}_e = \frac{1}{2}(g^{-2}\mathbf{F}_s^{-T}\mathbf{F}_s^{-1} - I). \quad (37)$$

Finally, we derive the equation of mass conservation in Eulerian coordinates. We assume, that homogeneous material with the same parameters is added, such that the density is constant $\hat{\rho}_g = \hat{\rho}_s^0$. Hence, if $m(\hat{V})$ is the mass of the reference state, $m(\hat{V}_g)$ is the mass of the grown material, which is conserved in the current configuration V

$$m(\hat{V}) = \int_{\hat{V}} \hat{\rho}_s^0 d\hat{\mathbf{x}}, \quad m(\hat{V}_g) = \int_{\hat{V}_g} \hat{\rho}_g d\hat{\mathbf{x}}^g = \hat{\rho}_s^0 \int_{\hat{V}} \hat{J}_g d\hat{\mathbf{x}} = \hat{\rho}_s^0 \int_V \hat{J}_g J_s d\mathbf{x}, \quad (38)$$

where $\hat{J}_g := \det(\hat{\mathbf{F}}_g) = \hat{g}^2$ is the determinant of the growth part, such that for the density ρ of the current configuration it holds

$$\rho = \hat{\rho} = g^2\hat{\rho}_s^0J_s. \quad (39)$$

3.2.2. Complete formulation in Eulerian coordinates

Variational Formulation 3 (Long-Scale, Fully Eulerian). Find the velocity $\mathbf{v}_f \in \bar{\mathbf{v}}^{in}(\tau) + \mathcal{V}_f$, deformation $\mathbf{u} \in \mathcal{W}_s$ and pressure $p_f \in \mathcal{L}_f$, such that

$$\begin{aligned} (\rho_f \mathbf{v}_f \cdot \nabla \mathbf{v}_f, \phi_f)_{\mathcal{F}(\tau)} + (\boldsymbol{\sigma}_f, \nabla \phi)_{\mathcal{F}(\tau)} + (J_g \boldsymbol{\sigma}_e \mathbf{F}_g^{-T}, \nabla \phi)_{\mathcal{S}(\tau)} &= 0 \quad \forall \phi \in \mathcal{W} \\ (\text{div } \mathbf{v}_f, \xi_f)_{\mathcal{F}(\tau)} &= 0 \quad \forall \xi_f \in \mathcal{L}_f. \end{aligned}$$

The elastic deformation gradient is defined in (35). Accumulation of foam cells is described by the ODE

$$\partial_\tau c_s = \gamma(\boldsymbol{\sigma}_{WS}, \tau).$$

The function spaces are defined as

$$\begin{aligned} \mathcal{V}_f &= [H_0^1(\mathcal{F}(\tau); \Gamma_i(\tau) \cup \Gamma_f^{in})]^2, & \mathcal{L}_f &= L^2(\mathcal{F}(\tau)), \\ \mathcal{W} &= [H_0^1(\Omega(\tau); \Gamma_f^{in} \cup \Gamma_s)]^2, & \mathcal{W}_s &= [H_0^1(\mathcal{S}(\tau); \Gamma_s^d)]^2. \end{aligned}$$

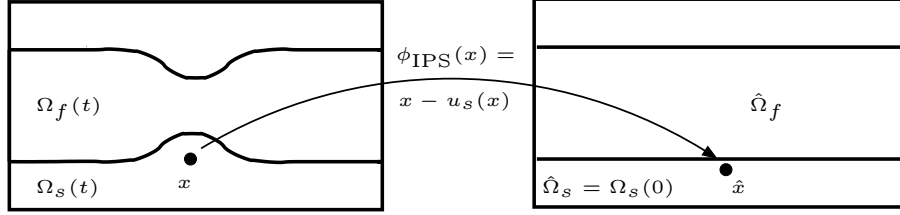


Figure 3: The Initial point set function Φ_{IPS} traces back points \mathbf{x} to their initial position in order to determine their domain affiliation.

The short-scale problem is given by

Variational Formulation 4 (Short-Scale, Fully Eulerian). For $\tau \geq 0$ days, Find the velocity $\mathbf{v} \in \mathbf{v}^{\text{in}}(t) + \mathcal{V}$, deformation $\mathbf{u} \in \mathcal{W}_s$ and pressure $p_f \in \mathcal{L}_f$, such that

$$\begin{aligned} (\rho_f(\partial_t \mathbf{v} + \mathbf{v} \cdot \nabla \mathbf{v}), \phi)_{\mathcal{F}(t)} + (J_s g^2 \hat{\rho}_s^0(\partial_t \mathbf{v} + \mathbf{v} \cdot \nabla \mathbf{v}), \phi)_{\mathcal{S}(t)} \\ + (\boldsymbol{\sigma}_f, \nabla \phi)_{\mathcal{F}(t)} + (J_g \boldsymbol{\sigma}_e \mathbf{F}_g^{-T}, \nabla \phi)_{\mathcal{S}(t)} = 0 \quad \forall \phi \in \mathcal{W} \\ (\text{div } \mathbf{v}_f, \xi_f)_{\mathcal{F}(t)} = 0 \quad \forall \xi_f \in \mathcal{L}_f, \\ (\partial_t \mathbf{u} + \mathbf{v} \cdot \nabla \mathbf{u} - \mathbf{v}, \psi_s)_{\mathcal{S}(t)} = 0 \quad \forall \psi_s \in \mathcal{W}_s, \end{aligned}$$

The elastic deformation gradient is defined in (35) and the growth function $g(\tau)$ is set constant within the short time scale. The function spaces are given as in the previous problem with exception of the global velocity space

$$\mathcal{V} = [H_0^1(\mathcal{F}(t) \cup \Gamma_i(t) \cup \mathcal{S}(t); \Gamma_f^{\text{in}} \cup \Gamma_s)]^2.$$

3.2.3. Interface capturing

The previous two variational formulations 3 and 4 are both of interface-capturing type. The two subproblems, fluid and solid, are given on the moving domains $\mathcal{F}(t)$ and $\mathcal{S}(t)$ that share a moving interface $\Gamma_i(t)$. To close the system, we have to specify an interface-capturing technique in order to decide whether a point \mathbf{x} belongs to the solid or the fluid domain. Therefore, we use the Initial Point Set (IPS) [19]. The IPS method makes use of the fact that a map between the current configuration $\mathcal{S}(t)$ and the initial domain $\mathcal{S}(0)$ is naturally given by the solid deformation u_s . This can be used in order to obtain the domain affiliation, see Figure 3. We define the IPS function

$$\Phi_{\text{IPS}}(\mathbf{x}, t) := \begin{cases} \mathbf{x} - \mathbf{u}_s(\mathbf{x}, t) & \mathbf{x} \in \mathcal{S}(t), \\ \mathbf{x} - \text{ext}(\mathbf{u}_s)(\mathbf{x}, t) & \mathbf{x} \in \mathcal{F}(t), \end{cases} \quad (40)$$

with a suitable extension operator from the solid domain $\mathcal{S}(t)$ to $\mathcal{F}(t)$. In practice, it is sufficient to define the extension in a small layer of fluid cells

near the interface [36, 35]. With the IPS function, we can decide the domain affiliation by the relation

$$\Phi_{\text{IPS}}(\mathbf{x}, t) \in \mathcal{S}(0) \Leftrightarrow \mathbf{x} \in \mathcal{S}(t). \quad (41)$$

In contrast to Level Set Methods [34] this can be done without solving an additional equation. Furthermore, the IPS method is also able to cope with sharp edges [19, 36].

4. Discretization

4.1. Temporal discretization

Temporal discretization is based on the Rothe method; i.e., the variational Formulations 2 and 4 are first discretized in time via a One-Step- θ scheme. Specifically, we choose in this paper $\theta = 1$, leading to the implicit A-stable backward Euler time-stepping scheme.

4.2. Spatial discretization of ALE-FSI

For discretization, we use a Galerkin finite element scheme on a mesh consisting of quadrilaterals. We use two different codes in order to test our developments. In Gascoigne 3d [4], we use equal-order finite elements with LPS-stabilization [3] for the ALE approach and edge stabilization [11] for the Eulerian approach. In deal.II [2] (using the fsi-template [45]), we employ the Q_2^c/P_1^{dc} element for the fluid part, which is inf-sup stable and locally mass conserving. Consequently, no pressure stabilization is needed. The solid is discretized with Q_2^c elements.

4.3. A locally modified finite element scheme for the fully Eulerian approach

For the Eulerian approach, we use a modified discretization scheme which is able to resolve the dynamics in the interface region accurately. Using interface capturing methods, the fluid-structure interface typically moves over a fixed background mesh. The mesh cells that are cut by the interface lie partly in the fluid domain, partly in the solid domain. Without further adjustment of the mesh or enrichment of the local finite element space, this leads to a poor approximation in the interface cells and may give rise to stability problems. To avoid these problems, we use a modified finite element scheme [22] in the interface cells. Our approach fits both into the frameworks of a fitted finite element approach and an enrichment strategy.

The key idea is to use a fixed background mesh consisting of patches $P \in \Omega_h$. Each patch that is not cut by the interface consists of 4 quadrilaterals. If it is cut by the interface, however, we divide the patch into 8 triangles in such a way that the interface is resolved properly, see Figure 4.

We have to distinguish between four cases (Figure 5): A patch might be cut at two opposite edges (A) or two adjacent edges (B). Furthermore, the cut might go through one edge and one vertex (C) or through two vertices (D). We adjust the edge midpoints and the midpoint of the cell in such a way that the interface is resolved in a linear approximation.

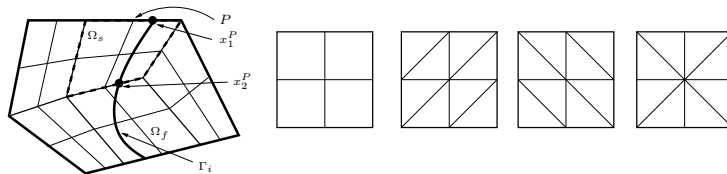


Figure 4: Left: triangulation Ω_h with interface Γ_i . Patch P is cut by Γ_i at x_1^P and x_2^P . Right: subdivision of reference patches $\hat{P}_1, \dots, \hat{P}_4$ into four quadrilaterals or eight triangles.

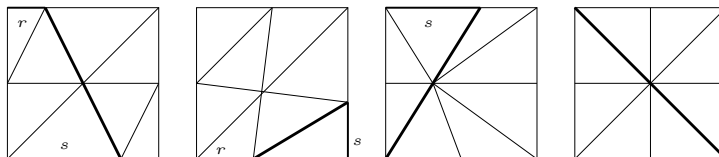


Figure 5: Different types of cut patches. From left to right: A , B , C and D . The subdivision can be anisotropic with $r, s \in (0, 1)$ arbitrary.

On this triangulation Ω_h^n , we define the finite element trial space $V_h \subset H_0^1(\Omega)$ as an iso-parametric space. If a patch is not cut by the interface, we use the standard space of bilinear functions (bilinear on each of the four sub-quads) for both reference element transformation and the finite element basis. If a patch $P \in \Omega_h$ however is cut, we use piecewise linear functions (linear on each of the eight triangles) for transformation and basis.

The arising cells can become arbitrarily anisotropic for $r, s \rightarrow 0, 1$ (Figure 5). We can guarantee, however, that a maximum angle condition remains valid. This enables us to show optimal error estimates of second order for elliptic problems [22]. No matter if the patch is cut or not, the local finite element approximation on each patch is defined by 9 local degrees of freedom. Therefore the total number of degrees of freedom and the structure and connectivity of the system matrix remain unchanged for all time steps.

5. Numerical Tests

In this final section, we test the proposed approaches. We compare the ALE approach with the fully Eulerian method as well as a temporal two-scale approach with a pure long-scale calculation. The objectives of these studies are threefold:

- Comparing the two variational approaches: ALE and fully Eulerian with respect to accuracy, convergence and ability to simulate large deformation;
- Showing the capability of the fully Eulerian approach to model closure;
- Investigation of a temporal two-scale algorithm and comparison with a simple long-scale calculation.

In Section 5.1 we start by discussing the long-scale case, Problem 1, only. Here, we will in particular analyze the coupled growth-fsi model and the convergence behavior of the different numerical schemes in certain functionals, such as wall deformation, vorticity and wall stress.

The long-scale problem uses an averaged inflow velocity profile and underestimates the wall stress in main stream direction. As this output directly enters the growth model, it has a significant impact on the coupled model. Hence, in Section 5.2, we propose a long-scale/short-scale algorithm, where subsequent runs of the short-scale problem, Problem 2, are included to achieve better estimates for the wall stress, entering the long-scale problem.

Problem setting

As geometry we use a channel of length 10 cm and an initial width $\omega(0)$ of 2 cm as illustrated in Figure 1. The solid parts on the top and bottom have an initial thickness of 1 cm each. Fluid density and viscosity are given by $\rho_f = 1 \text{ g/cm}^3$ and $\nu_f = 0.3 \text{ cm}^2/\text{s}$. The solid parameters are given by $\rho_s = 1 \text{ g/cm}^3$ and the Lamé parameters $\mu_s = 10^4$ and $\lambda_s = 4 \cdot 10^4 \text{ dyn/cm}^2$. We prescribe a pulsating velocity inflow profile on Γ_f^{in} given by

$$\mathbf{v}^{\text{in}}(t, x, y) = \frac{3}{2} \begin{pmatrix} \mathbf{v}^{\text{in}}(t)(1 - y^2) \\ 0 \end{pmatrix}, \quad \mathbf{v}^{\text{in}}(t) = (\varepsilon_\omega + 5\omega(t))(1 + \sin(2\pi t))\text{cm/s}, \quad (42)$$

depending on the minimal width of the channel $\omega(t)$ (see Figure 1). The parameter ε_ω is used to control the minimum flow rate and will be specified below. These parameters are chosen such, that the temporal dynamics of the coupled problem are close to a real plaque growth situation. The remaining boundary conditions are specified in (5) and (7). For the growth, we specify a function that depends on the concentration of foam cells c_s that is defined by the ODE (2). We assume that growth is centered around the middle part of the vessel

$$\hat{g}(\hat{x}, \hat{y}, \tau) = 1 + c_s(\tau) \exp\left(-\hat{x}^2\right)(2 - |\hat{y}|), \quad \hat{\mathbf{F}}_g(\hat{x}, \hat{y}, \tau) := \hat{g}(\hat{x}, \hat{y}, \tau) \mathbf{I}. \quad (43)$$

Growth \hat{g} and inflow rate \mathbf{v}^{in} depend implicitly on the solution. As the configuration is symmetric in the vertical direction, we can restrict the simulation domain to the lower half of the geometry.

5.1. Long-Scale Problem

The long-scale problem is driven by a parabolic inflow profile with an average inflow rate $\bar{\mathbf{v}}^{\text{in}}(\tau)$. We use the averaged inflow profile (42):

$$\bar{\mathbf{v}}^{\text{in}}(\tau) = (\varepsilon_\omega + 5\omega(\tau))\text{cm/s}. \quad (44)$$

We discretize the coupled system by a splitting in time and approximate the long-scale problem by the following iteration:

Algorithm 1: Long-Scale Iteration

Initialize $\mathbf{v}^0 = 0$, $\mathbf{u}^0 = 0$, $g^0 = 0$ and the vessel-width $\omega^0 = 2$. Set time-step $k_l = 0.1$ days = 8 640 s. Iterate for $n = 1, 2, \dots$:

1. Solve quasi-stationary Long-Scale Problem 1:

$$\{c_s^{n-1}, \omega^{n-1}\} \mapsto \{\mathbf{v}^n, \mathbf{u}^n, p^n\}$$

2. Compute the vessel width in point $A(\tau_n)$

$$\omega^n = 2 - 2\mathbf{u}_{s,2}^n(A(\tau_n), \tau_n)$$

3. Compute the wall stress in main stream direction

$$\sigma_{WS}^n = \int_{\Gamma_i} |\boldsymbol{\sigma}_f(\mathbf{v}^n, p^n) \vec{n} \cdot \vec{e}_1| d\sigma \quad (45)$$

4. Update the foam cell concentration

$$c_s^n = c_s^{n-1} + k_l \gamma_0 (1 + \sigma_{WS}^n / \bar{\sigma})^{-1}$$

Here and in the following $\mathbf{u}_{s,2}$ denotes the second (vertical) component of the solid displacement \mathbf{u}_s .

5.1.1. Long-Scale with $\varepsilon_\omega = 0.1$ cm/s

For our first study we choose a minimum inflow velocity of $\varepsilon_\omega = 0.1$ cm/s. At first, we compare results obtained with the fully Eulerian approach on a grid with 4096 patches with results obtained by an ALE approach on a grid with 2560 patches. In Figure 6 we show the course of different functionals over time: the wall stress in main stream direction on the vessel wall Γ_i (45), the channel width $\omega(\tau_n) = 2 - 2\mathbf{u}_{s,2}(A(\tau_n))$ in the center of growth $A(\tau_n)$ (see Figure 1), the vorticity of the solution in the L^2 -norm and the outflow at the right boundary defined by

$$J_{\text{vort}} = \int_{\mathcal{F}(\tau)} (\partial_y \mathbf{v}_1 - \partial_x \mathbf{v}_2)^2 d\mathbf{x}, \quad J_{\text{out}} = \int_{\Gamma_{f,\text{out}}} \mathbf{v} \cdot \mathbf{n} d\sigma. \quad (46)$$

The functional values for the ALE method (harmonic and biharmonic extension) and the fully Eulerian approach show very good agreement. Using the harmonic extension, the ALE method broke down at $\tau = 63.2$ days due to degeneration of mesh cells, with the biharmonic extension, we were able to obtain results up to $\tau = 109.3$ days.

The fully Eulerian method, on the other hand, was able to yield reliable results until the channel was almost closed. As the inflow velocity is bounded from below by $\varepsilon_\omega = 0.1$ cm/s and as the fluid is incompressible, a passage must always remain. As higher wall stresses slow down plaque growth, see (2), the vertical displacement approaches a limit. However, increasing fluid-dynamical

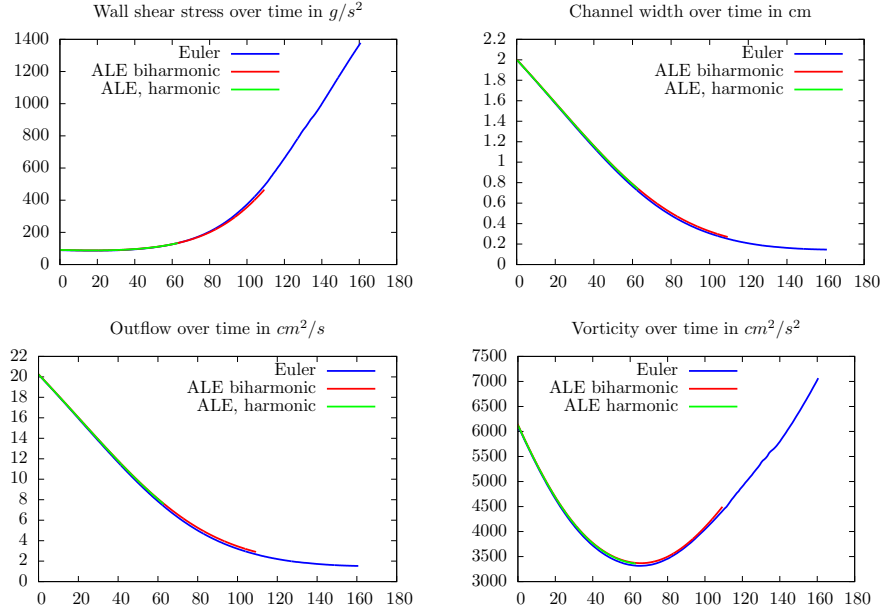


Figure 6: Long-Scale Problem: Course of different functionals over time (in days). *Top left:* Averaged wall stress σ_{WS} in g/s^2 . *Top right:* Channel width in cm. *Bottom left:* Outflow $v \cdot \vec{n}$ over $\Gamma_{f,out}$ in cm^2/s . *Bottom right:* Averaged vorticity in cm^2/s^2 .

forces cause strong horizontal deflections that finally result in a break-down of the simulation at time $t = 160.1$ days.

As the results for the ALE method with harmonic and biharmonic extension are nearly identical until time $\tau = 63.1$ days, we will not show the harmonic variant anymore in the following tests.

In Figure 7, we show the deformed meshes at time $\tau = 109.3$ days for the ALE approach with biharmonic mesh deformation and the fully Eulerian approach. In the case of the biharmonic ALE approach, this was the last mesh before the calculation broke down.

Next, we study convergence with respect to the spatial grid size h for both the fully Eulerian and the ALE technique in Table 1. For the fully Eulerian approach, we use Q_1 equal-order elements and meshes with 256, 1024 and 4096 patch elements. For the ALE approach we use Q_2^s/P_1^{dc} elements and choose slightly coarser meshes for a fair comparison.

We evaluate the functionals at $\tau = 50$ days. The functional values for the ALE and the fully Eulerian approach converge roughly against the same values. Small differences are due to time discretization (the time step has been chosen 0.1 days) and the fact that in the ALE method, the deformation enters implicitly which means that the deformation u^n at time τ_n defines the domains $\mathcal{F}^n, \mathcal{S}^n$, while in the fully Eulerian method, we apply the deformation explicitly, which means that the deformation u^n at time τ_n determines the domains $\mathcal{F}^{n+1}, \mathcal{S}^{n+1}$.

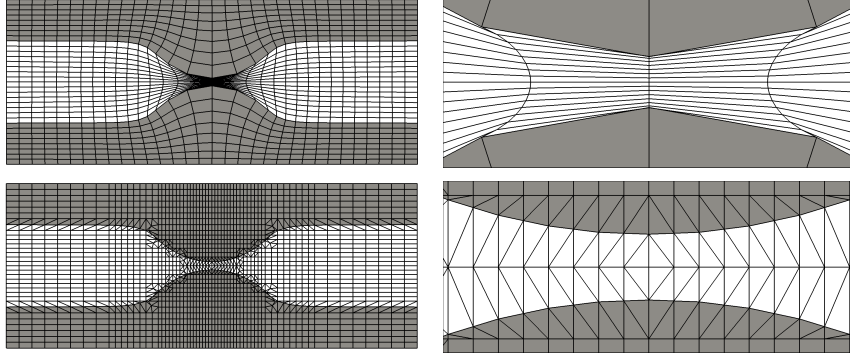


Figure 7: Biharmonic deformation (on top) close to break-down at $\tau = 109.3$ days and zoom-in at right. On the bottom the corresponding meshes at the same time instance $\tau = 109.3$ days for the fully Eulerian approach are provided.

#patches	Wall Stress	Width	Vorticity	Outflow
Euler 256	$1.033 \cdot 10^2$	1.092	$3.408 \cdot 10^3$	9.251
1024	$1.050 \cdot 10^2$	1.064	$3.457 \cdot 10^3$	9.547
4096	$1.060 \cdot 10^2$	1.052	$3.472 \cdot 10^3$	9.648
Extrapol.	$1.074 \cdot 10^2$	1.047	$3.479 \cdot 10^3$	9.700
Conv.	0.77	1.81	1.71	1.55
ALE 160	$1.087 \cdot 10^2$	1.033	$3.527 \cdot 10^3$	9.892
640	$1.076 \cdot 10^2$	1.037	$3.515 \cdot 10^3$	9.849
2560	$1.073 \cdot 10^2$	1.038	$3.510 \cdot 10^3$	9.834
Extrapol.	$1.072 \cdot 10^2$	1.039	$3.506 \cdot 10^3$	9.826
Conv.	1.87	1.49	1.26	1.52

Table 1: Convergence of functional values at $t = 50$ days on three different grids for the fully Eulerian and the ALE approach. We indicate estimated convergence rates and extrapolated values.

in the next time step.

Furthermore, we estimate the convergence order for all of the functionals, see Table 1. Besides the wall stress, all estimated convergence orders lie between linear and quadratic convergence and the ALE and the fully Eulerian approach converge similarly. The ALE approach, however, seems to yield better values already on very coarse grids. Furthermore, the ALE approach shows faster convergence in the wall stress functional. The reason for this better performance is the use of inf-sup stable Q_2/P_1^{dc} elements in the case of ALE, which is not yet possible with the parametric interface approximation scheme described in Section 4.3, where stabilized $Q_1 - Q_1$ elements are used.

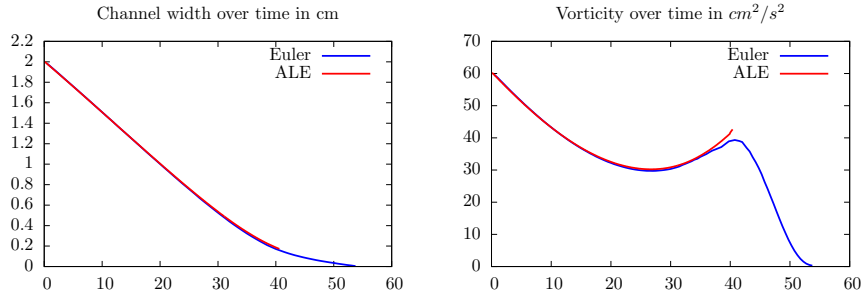


Figure 8: Channel width and vorticity for a long-scale simulation with reduced inflow velocity. The inflow velocity goes to zero when the channel closes. This makes the complete closure of the channel possible.

5.1.2. Long-Scale with $\varepsilon_\omega = 0$ cm/s

An interesting aspect from a modeling point of view is the question of whether the channel closes completely or whether a small layer of fluid remains between the vessel walls. As discussed before, a complete closure of the channel is not possible as long as the inflow rate ε_ω is positive.

To study closure, we decrease the minimal inflow velocity ε_ω from 0.1 to 0 and the velocity inflow by a factor of 10 to

$$\mathbf{v}_1^{\text{in}}(\tau) = 0.15 \cdot (5\omega(\tau))(1 - y^2) \text{ cm/s.} \quad (47)$$

In this configuration, the flow through the narrow part of the channel will be considerably smaller when the channel is almost closed. This has two important effects: First, fluid forces acting against the growth of the solid are much smaller. Secondly, the wall stress becomes smaller which has a strengthening impact on the solid growth in our model. Altogether, this has the effect that the growth is much faster. Furthermore, in our simulation the channel closes completely at time $\tau = 55.8$ days.

In Figure 8, we show plots of the channel width and the vorticity over time. In contrast to the larger inflow velocity studied above, the fluid forces (e.g. the vorticity) decrease after $\tau \approx 40$ days which makes the closure of the channel possible. In Figure 9, we show the last mesh obtained with the fully Eulerian approach ($\tau = 55.8$ days) where the channel is completely closed. The ALE calculation (with biharmonic extension) broke down at time $\tau = 40.6$ days.

5.2. Long-Scale/Short-Scale Problem with $\varepsilon_\omega = 0.1$ cm/s

In the previous section, we have advanced the growth-function (2) by

$$c_s^n = c_s^{n-1} + k\gamma_0(1 + \sigma_{WS}^n/\bar{\sigma})^{-1}, \quad (48)$$

where σ_{WS}^n is the wall stress in main stream direction estimated from the quasi-stationary fsi-solution at time τ_n that was obtained using the averaged inflow profile (42). We will see, that this value is only a very coarse prediction compared

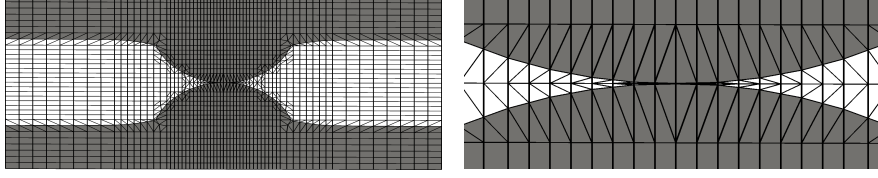


Figure 9: Example 5.1.2: Fully Eulerian deformation when the channel is completely closed at $\tau = 55.8$ days.

to the averaged wall stress of the short-scale problem. Hence, to enhance the quality of the coupled solution, we propose and study the following algorithm:

Algorithm 2: Long-Scale/Short-Scale Iteration

Initialize $\mathbf{v}^0 = 0$, $\mathbf{u}^0 = 0$, $g^0 = 0$ and the vessel-width $\omega^0 = 2$. Set time-step $k_l = 1 \text{ day} = 86\,400 \text{ s}$. Iterate for $n = 1, 2, \dots$:

1.a) Solve quasi-stationary Long-Scale Problem 1:

$$\{c_s^{n-1}, \omega^{n-1}\} \mapsto \{\mathbf{v}^n, \mathbf{u}^n, p^n\}$$

1.b) Compute the vessel width in the point $A(\tau_n)$

$$\omega^n = 2 - 2\mathbf{u}_{s,2}^n(A(\tau_n), \tau_n)$$

2.a) Set $\mathbf{v}^{s,0} = \mathbf{v}^n$, $\mathbf{u}^{s,0} = \mathbf{u}^n$ and solve the short-scale problem 2 in $I_n = [\tau_n \text{ days}, \tau_n \text{ days} + 1 \text{ s}]$

$$\{\mathbf{v}^{s,0}, \mathbf{u}^{s,0}, c_s^{n-1}, \omega^n\} \mapsto \{\mathbf{v}^{s,m}, \mathbf{u}^{s,m}, p^{s,m}\}, m = 1, \dots, N_s$$

2.b) Compute average wall stress in main stream direction

$$\sigma_{WS}^n = \frac{1}{N_s} \sum_{m=1}^{N_s} \int_{\Gamma_i} |\boldsymbol{\sigma}_f(\mathbf{v}^{s,m}, p^{s,m}) \vec{n} \cdot \vec{e}_1| d\mathbf{o}$$

2.c) Update the foam cell concentration

$$c_s^n = c_s^{n-1} + k_l \gamma_0 (1 + \sigma_{WS}^n / \bar{\sigma})^{-1}$$

Remark 4 (Long-Scale - Long-Scale/Short-Scale). *The only difference between the two algorithms is the computation of the wall stress. In Section 5.1, σ_{WS}^n is computed based on the long-scale solution using an averaged inflow velocity $\bar{\mathbf{v}}^{in}$, whereas in the present section, the wall stress is computed as average of the short-scale solution in $I_n = [\tau_n \text{ days}, \tau_n \text{ days} + 1 \text{ s}]$ using a pulsating flow. We expect (and see) differences, as the dependency of the wall stress on the inflow*

profile is strongly nonlinear, such that the kind of averaging has an impact. Due to the high computational cost of the non-stationary small-scale problem, which has to be solved once in every long-scale step, we enlarge the step-size of the long-scale problem to $k = 1$ day. Using $k_s = 0.02$ s for the short-scale problem, 50 time-steps are required to evaluate a prediction of the wall stress in every cycle.

Remark 5. Algorithm 2 can be considered as a staggered partitioned approximation to the coupled problem. The quasi-stationary long-scale problem in Step 1.a), i.e. the propagation of the plaque growth, is solved by explicitly using the foam cell concentration from the last time-step. Then, in Step 2.a), a new prediction of the effective wall stress is solved by neglecting the propagation of the foam cell concentration. Regarding the very short time-span of some seconds used to predict this short-term effects, this simplification is adequate. An improvement of this algorithm is possible by iterating the two sub-steps of the Algorithm. This would increase the stability of the resulting scheme and furthermore allow to use second-order time-stepping methods for the two sub-problems. This, however, is subject to ongoing research.

5.2.1. Analysis of the Short-Scale problem

We start the analysis by comparing the effect of the short-scale stress prediction. In Figure 10 we show the dynamic wall stress over three cycles of the heart beat $\delta t = 3$ s. The channel width was taken from the long-term simulation at time $\tau = 50$ days. Initial values for $\mathbf{v}_s, \mathbf{u}_s, \omega$ and c_s have been calculated in advance by solving the long-scale problem. The minimum inflow velocity is again set to $\varepsilon_\omega = 0.1$ cm/s as in Section 5.1.1. In Figure 10, we compare the average of the wall stress as estimated from the dynamic short-term simulation with the wall stress coming from the long-term simulation. It turns out that using the long-term value, we have an underestimation of about 30%. The short-term results differ only marginally between the ALE and the Eulerian formulation.

In Table 2, we study convergence of the short-scale problem with respect to time discretization. We compare the locally computed mean wall stress calculated by one cycle $I_n = [\tau_n \text{ days}, \tau_n \text{ days} + 1 \text{ s}]$ of the periodic inflow to the mean calculated from 3 cycles $I_n = [\tau_n \text{ days}, \tau_n \text{ days} + 3 \text{ s}]$ and for both the ALE and the fully Eulerian method. The values for 1 and 3 cycles differ by 1.8% and 2.8%. Considering the computational cost of these short-scale computations, it seems justifiable to use only one cycle for a full long-scale/short-scale calculation. We note that this short averaging period might not be enough in the case of a more complex growth model or a full three dimensional configuration. The values obtained for ALE calculations and the fully Eulerian approach are also within reasonable agreement.

5.2.2. Analysis of the coupled Long-Scale/Short-Scale problem

Finally, we compare the pure long-scale strategy with the two-scale approach in a long-term simulation. In Figure 11, we plot the channel width and the wall stress over time. As mentioned above, the pure Long-Scale approach

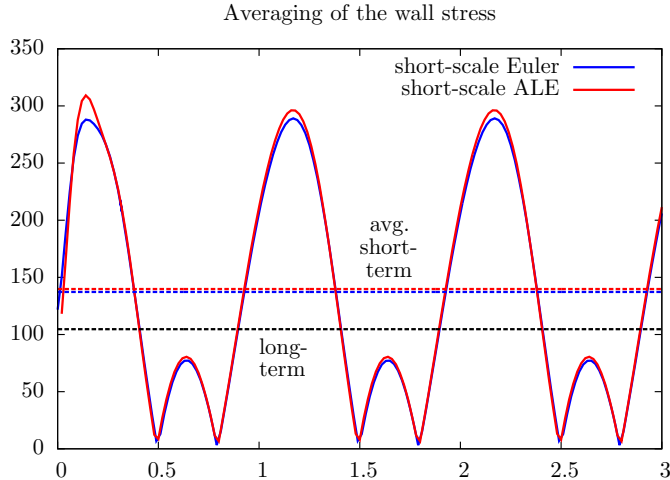


Figure 10: Dynamic wall stresses of the short-term problem and average values (dashed red and blue lines). Comparison with the wall stress of the long-term problem (dashed black line).

dt	Euler, 1 cycle	Euler, 3 cycles	ALE, 1 cycle	ALE, 3 cycles
0.04	$1.353 \cdot 10^2$	$1.379 \cdot 10^2$	$1.379 \cdot 10^2$	$1.409 \cdot 10^2$
0.02	$1.348 \cdot 10^2$	$1.372 \cdot 10^2$	$1.358 \cdot 10^2$	$1.398 \cdot 10^2$
0.01	$1.342 \cdot 10^2$	$1.367 \cdot 10^2$	$1.354 \cdot 10^2$	$1.389 \cdot 10^2$

Table 2: Local wall stress, computed from short-scale computations with the ALE and fully Eulerian approach and for one cycle $I_n = [\tau_n \text{ days}, \tau_n \text{ days} + 1 \text{ s}]$ and 3 cycles $I_n = [\tau_n \text{ days}, \tau_n \text{ days} + 3 \text{ s}]$ each.

underestimates the wall stress in the beginning. Thus, the solid grows significantly faster (which on the other hand has a positive effect on the wall stress such that the plots cross at $\tau \approx 70$ days). A bisection of the channel width is reached at $\tau \approx 56$ days when using the coupled model compared to $\tau \approx 48$ days when using the pure Long-Scale approach in Section 5.1.1. This is a discrepancy of 17%.

As seen before, the channel width reaches a limit $\omega(\tau) \approx 0.15$ cm at $\tau \approx 160$ days. With the two-scale approach, the channel closes slower and a limit is reached at $\tau \approx 190$ days with a channel width $\omega(\tau) \approx 0.11$ cm. Again, the ALE and the fully Eulerian method show reasonable agreement up to the time where the ALE mesh degenerates.

6. Conclusions

In this article, we first developed two schemes for mechano-chemical fluid-structure interactions with active solid growth in terms of the ALE and the

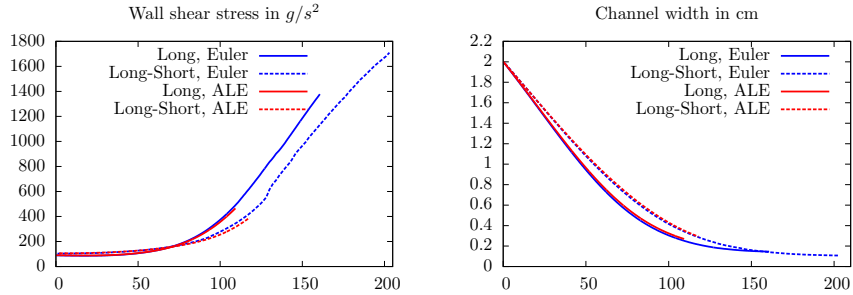


Figure 11: Comparison of pure long-scale computations with the Long-Scale/Short-Scale iteration. We compare wall stress and the channel width over time. The pure long-scale approach underestimates the wall stress in the beginning such that the channel closes faster.

fully Eulerian approach. We could show that both approaches are in very good agreement in the case of moderate growth and deformation. Where the emphasis is on closure and contact, the fully Eulerian formulation provides an elegant way in modeling using a fully monolithic setting. We demonstrate that, without remeshing techniques, ALE simulations suffer from mesh degeneration. Even by using a costly biharmonic mesh motion technique, monolithic ALE approaches fail.

Secondly, we introduced an efficient two-scale approach to simulate long-term processes with consideration of short-scale effects, where the latter cannot be resolved in detail. By incorporating effective parameters from small-scale computations in the long-scale problem, we obtained a significant variation in the coupled dynamics. Applying this two-scale approach to a plaque formation model, we could show a decrease of the growth rate by 17%. In contrast to this variation, discrepancies coming from different discretization techniques used for the ALE and the fully Eulerian approach are of lesser importance.

The studies presented in this paper are prototypical. It should be emphasized that the Eulerian approach can directly be applied to various large-deformation fluid-structure interaction and also mechano-chemical FSI problems. To tackle practical problems, the extension to 3D configurations will be necessary. From a modeling point of view, this is straightforward for both the ALE and the fully Eulerian approach. However, the extension of the locally modified finite element scheme as well as the computational complexity will be a particular challenge.

Finally, temporal splitting schemes are of great importance in various applications such as weathering processes. This work contributes to further development into this direction.

References

References

- [1] Ambrosi, D., Ateshian, G., Arruda, E., Cowin, S., Dumais, J., Goriely, A., Holzapfel, G., Humphrey, J.D., Kemkemer, R., Kuhl, E., Olberding, J., Taber, L., Garikipati, K.: Perspectives on biological growth and remodeling. *J. Mech. Phys. Solids* **59**(4), 863–883 (2011)
- [2] Bangerth, W., Heister, T., Heltai, L., Kanschat, G., Kronbichler, M., Maier, M., Turcksin, B., Young, T.D.: The `deal.II` library, version 8.2. *Archive of Numerical Software* **3** (2015)
- [3] Becker, R., Braack, M.: A finite element pressure gradient stabilization for the Stokes equations based on local projections. *Calcolo* **38**(4), 173–199 (2001)
- [4] Becker, R., Braack, M., Meidner, D., Richter, T., Vexler, B.: The finite element toolkit GASCOIGNE. [HTTP://WWW.GASCOIGNE.UNI-HD.DE](http://www.gascoigne.uni-hd.de)
- [5] Boffi, D., Gastaldi, L.: A finite element approach for the immersed boundary method. *Computers & structures* **81**(8), 491–501 (2003)
- [6] Braack, M., Ern, A.: Coupling multimodeling with local mesh refinement for the numerical solution of laminar flames. *Combust. Theory Modelling* **8**(4), 771–788 (2004)
- [7] Bulezai, M., Dubbeldam, J.: Long time evolution of atherosclerotic plaques. *J. Theor. Biol.* **297**, 1–10 (2012)
- [8] Bungartz, H.J., Mehl, M., Schäfer, M.: Fluid-Structure Interaction II: Modelling, Simulation, Optimization. *Lecture Notes in Computational Science and Engineering*. Springer (2010)
- [9] Bungartz, H.J., Schäfer, M.: Fluid-Structure Interaction: Modelling, Simulation, Optimization, *Lecture Notes in Computational Science and Engineering*, vol. 53. Springer (2006)
- [10] Burman, E., Fernández, M.A.: An unfitted Nitsche method for incompressible fluid–structure interaction using overlapping meshes. *Computer Methods in Applied Mechanics and Engineering* **279**, 497 – 514 (2014)
- [11] Burman, E., Hansbo, P.: Edge stabilization for the generalized stokes problem: a continuous interior penalty method. *Computer methods in applied mechanics and engineering* **195**(19), 2393–2410 (2006)
- [12] Causin, P., Gerbeau, J.F., Nobile, F.: Added-mass effect in the design of partitioned algorithms for fluid-structure problems. *Comput. Methods Appl. Mech. Engrg.* **194**, 4506–4527 (2005)

- [13] Chen, C., Ding, Y., Gear, J.: Numerical simulation of atherosclerotic plaque growth using two-way fluid-structural interaction. *ANZIAM J.* **53**, 278–291 (2012)
- [14] Ciarlet, P.G.: *Mathematical Elasticity. Volume 1: Three Dimensional Elasticity.* North-Holland (1984)
- [15] Cilla, M., na, E.P., Martínez, M.: Mathematical modelling of atheroma plaque formation and development in coronary arteries. *J. R. Soc. Interface* **11**(90) (2013)
- [16] Cottet, G.H., Maitre, E., Milcent, T.: Eulerian formulation and level set models for incompressible fluid - structure interaction. *Math. Modell. Numer. Anal.* **42**, 471–492 (2008)
- [17] Donea, J.: An arbitrary lagrangian-eulerian finite element method for transient dynamic fluid-structure interactions. *Comput. Methods Appl. Mech. Engrg.* **33**, 689–723 (1982)
- [18] Donea, J., Huerta, A., Ponthot, J.P., Rodríguez-Ferran, A.: *Arbitrary Lagrangian–Eulerian Methods.* John Wiley & Sons, Ltd (2004)
- [19] Dunne, T.: An Eulerian approach to fluid-structure interaction and goal-oriented mesh refinement. *Int. J. Numer. Math. Fluids.* **51**, 1017–1039 (2006)
- [20] Dunne, T., Rannacher, R., Richter, T.: Numerical simulation of fluid-structure interaction based on monolithic variational formulations. In: G. Galdi, R. Rannacher (eds.) *Comtemporary Challenges in Mathematical Fluid Mechanics.* World Scientific, Singapore (2010)
- [21] Formaggia, L., Quarteroni, A., Veneziani, A.: *Cardiovascular Mathematics: Modeling and simulation of the circulatory system.* Springer-Verlag, Italia, Milano (2009)
- [22] Frei, S., Richter, T.: A locally modified parametric finite element method for interface problems. *SIAM J. Numer. Anal.* (2014)
- [23] Gerstenberger, A., Wall, W.A.: An extended finite element method/lagrange multiplier based approach for fluid-structure interaction. *Computer Methods in Applied Mechanics and Engineering* **197**(19-20), 1699–1714 (2008)
- [24] Hansbo, A., Hansbo, P.: A finite element method for the simulation of strong and weak discontinuities in solid mechanics. *Comput. Methods Appl. Mech. Engrg.* **193**(33-35), 3523–3540 (2004)
- [25] Hansbo, P., Hermansson, J., Svedberg, T.: Nitsche’s method combined with space–time finite elements for ale fluid – structure interaction problems. *Comput. Methods Appl. Mech. Engrg.* **193**(39-41), 4195–4206 (2004)

- [26] Holzapfel, G.: *Nonlinear Solid Mechanics: A Continuum Approach for Engineering*. Wiley-Blackwell (2000)
- [27] Hughes, T., Liu, W., Zimmermann, T.: Lagrangian-eulerian finite element formulations for incompressible viscous flows. *Computer Methods in Applied Mechanics and Engineering* **29**, 329–349 (1981)
- [28] Humphrey, J.: Vascular mechanics, mechanobiology and remodeling. *J. Mech. Med. Biol.* **9**(2), 243–257 (2009)
- [29] Janela, J., Moura, A., Sequeira, A.: Absorbing boundary conditions for a 3d non-Newtonian fluid-structure interaction model for blood flow in arteries. *Int. J. Engrg. Sci.* (2010)
- [30] Jones, G., Chapman, S.: Modeling growth in biological materials. *SIAM Review* **54**(1), 52–118 (2012)
- [31] Laadhari, A., Ruiz-Baier, R., Quarteroni, A.: Fully eulerian finite element approximation of a fluid-structure interaction problem in cardiac cells. *Int. J. Numer. Methods Engrg.* **96**, 712–738 (2013)
- [32] Legay, A., Chessa, J., Belytschko, T.: An eulerian-lagrangian method for fluid-structure interaction based on level sets. *Comp. Methods Appl. Mech. Engrg.* **195**, 2070–2087 (2006)
- [33] Moes, N., Dolbow, J., Belytschko, T.: A finite element method for crack growth without remeshing. *Int. J. Numer. Meth. Engrg.* **46**, 131–150 (1999)
- [34] Osher, S., Sethian, J.: Fronts propagating with curvature-dependent speed: algorithms based on Hamiltonian-Jacobi formulations. *J. Comput. Phys.* **79**(1), 12–49 (1988)
- [35] Richter, T.: A fully Eulerian formulation for fluid-structure interaction problems. *J. Comput. Phys.* **233**, 227–240 (2012)
- [36] Richter, T., Wick, T.: Finite elements for fluid-structure interaction in ALE and fully Eulerian coordinates. *Comp. Methods Appl. Mech. Engrg.* **199**, 2633–2642 (2010)
- [37] Rodriguez, E., Hoger, A., McCulloch, A.: Stress-dependent finite growth in soft elastic tissues. *J. Biomechanics* **4**, 455–467 (1994)
- [38] Stein, K., Tezduyar, T., Benney, R.: Mesh moving techniques for fluid-structure interactions with large displacements. *J. Appl. Mech.* **70**, 58–63 (2003)
- [39] Sugiyama, K., Ii, S., Takeuchi, S., Takagi, S., Matsumoto, Y.: A full eulerian finite difference approach for solving fluid-structure coupling problems. *J. Comp. Phys.* **3**(0), 596–627 (2011)

- [40] Tezduyar, T., Behr, M., Liou, J.: A new strategy for finite element computations involving moving boundaries and interfaces - the deforming-spatial-domain/space-time procedure: I. the concept and the preliminary numerical tests. *Comp. Methods Appl. Mech. Engrg.* **94**, 339–351 (1992)
- [41] Tezduyar, T., Behr, M., Mittal, S., Liou, J.: A new strategy for finite element computations involving moving boundaries and interfaces - the deforming-spatial-domain/space-time procedure: II. Computation of free-surface flows, two-liquid flows, and flows with drifting cylinders. *Comp. Methods Appl. Mech. Engrg.* **94**, 353–371 (1992)
- [42] Van Epps, J., Vorp, D.: Mechanopathobiology of atherogenesis: a review. *J. Surg. Research* **142**, 202–217 (2007)
- [43] Wick, T.: Fluid-structure interactions using different mesh motion techniques. *Computers and Structures* **89**, 1456–1467 (2011)
- [44] Wick, T.: Fully Eulerian fluid-structure interaction for time-dependent problems. *Comp. Methods Appl. Mech. Engrg.* **255**(0), 14–26 (2012). DOI 10.1016/j.cma.2012.11.009
- [45] Wick, T.: Solving monolithic fluid-structure interaction problems in arbitrary Lagrangian Eulerian coordinates with the deal.ii library. *Archive of Numerical Software* **1**, 1–19 (2013). URL <http://www.archnumsoft.org>
- [46] Wick, T.: Flapping and contact FSI computations with the fluid-solid interface-tracking/interface-capturing technique and mesh adaptivity. *Computational Mechanics* **53**(1), 29–43 (2014)
- [47] Wick, T.: Variational-monolithic ale fluid-structure interaction: Comparison of computational cost and mesh regularity using different mesh motion techniques (2016). Accepted for HPSC Hanoi proceedings; RICAM preprint 2016-12 online on <http://www.ricam.oeaw.ac.at/publications/ricam-reports/>
- [48] Xu, Z., Chen, N., Shadden, S.C., Marsden, J.E., Kamocka, M.M., Rosen, E.D., Alber, M.: Study of blood flow impact on growth of thrombi using a multiscale model. *Soft Matter* **5**, 769–779 (2009)
- [49] Yang, Y.: Mathematical modeling and simulation of the evolution of plaques in blood vessels. Doktorarbeit, Institut für Angewandte Mathematik, Universität Heidelberg, urn:nbn:de:bsz:16-heidok-164255 (2014)
- [50] Yang, Y., Jäger, W., Neuss-Radu, M., Richter, T.: Mathematical modeling and simulation of the evolution of plaques in blood vessels. *J. of Math. Biology* **72**, 973–996 (2016)
- [51] Yang, Y., Richter, T., Jäger, W., Neuss-Radu, M.: An ale approach to mechano-chemical processes in fluid-structure interactions. *Int. J. Numer. Math. Fluids*. (submitted, 2015)